JAERI-M--91-026

JP9105059

JAERI-M
91-026

LOCAL TRANSPORT ANALYSIS OF L-MODE PLASMAS IN JT-60 TOKAMAK

March 1991

Toshio HIRAYAMA, Mitsuru KIKUCHI, Hiroshi SHIRAI
Katsuhiro SHIMIZU, Masatoshi YAGI, Yoshihiko KOIDE
Shinichi ISHIDA and Masafumi AZUMI

日 本 原 子 力 研 究 所
Japan Atomic Energy Research Institute

JAERI-Mレポートは，日本原子力研究所が不定期に公刊している研究報告書です．
入手の問合わせは，日本原子力研究所技術情報部情報資料課（〒319-11茨城県那珂郡東海村）あて，お申しこしください．なお，このほかに財団法人原子力弘済会資料センター（〒319-11茨城県那珂郡東海村日本原子力研究所内）で複写による実費頒布をおこなっております

JAERI-M reports are issued irregularly.
Inquiries about availability of the reports should be addressed to Information Division, Department of Technical Information, Japan Atomic Energy Research Institute, Tokai-mura, Naka-gun, Ibaraki-ken 319-11, Japan.

編集兼発行　日本原子力研究所
印　　刷　株原子力資料サービス

JAERI-M 91-026

Local Transport Analysis of L-mode Plasmas in JT-60 Tokamak

Toshio HIRAYAMA, Mitsuru KIKUCHI, Hiroshi SHIRAI
Katsuhiro SHIMIZU, Masatoshi YAGI, Yoshihiko KOIDE
Shinichi ISHIDA and Masafumi AZUMI

Department of Large Tokamak Research
Naka Fusion Research Establishment
Japan Atomic Energy Research Institute
Naka-machi, Naka-gun, Ibaraki-ken

(Received February 4, 1991)

Local heat transport has been studied in auxiliary heated JT-60 plasmas with emphasis on understanding the deteriorated confinement observed in L-mode plasmas. The systematic experiment and analysis have been carried out in L-mode phase of divertor (single null, lower X-point), and limiter discharges with hydrogen neutral beam heating into hydrogen plasmas, based on sets of consistent experimental data including ion temperature profiles from CXR measurements. The deterioration in the energy confinement time with increasing the auxiliary heating power, so-called the power scaling, is mainly due to the degradation in ion energy transport. The confinement improvement as the plasma current increases is followed by both improvement in ion and electron transport properties. It is found that the ion thermal diffusivity has an approval dependence on the density. High ion temperature ($T_i(0) \leq 12$ keV) L-mode plasmas are attained at high β_p up to 3.5. The centrally peaked ion temperature is significantly due to the improvement in ion transport property, which is reduced to the level of the electron thermal diffusivities.

Keywords: JT-60, Tokamak, L-mode, Transport, Thermal diffusivity, High-Ti, Neutral Beam Heating

JT-60におけるLモードプラズマの局所熱輸送解析

日本原子力研究所那珂研究所臨界プラズマ研究部
平山 俊雄・菊池 満・白井 浩
清水 勝宏・矢木 雅敏・小出 芳彦
石田 真一・安積 正史

(1991年2月4日受理)

Lモードプラズマの閉じ込め特性が劣化する原因を明かにするために，JT-60の追加熱時のプラズマの局所的熱輸送解析を行った。輸送解析に必要なCXR測定によるイオン温度分布をはじめとする詳細な分布計測を，リミター放電，ダイバータ放電に関して系統的に行い，JT-60の広範なパラメータ領域について，Lモードプラズマの輸送特性を明かにした。通常，パワー依存性と呼ばれる，加熱パワーの増大に伴う閉じ込め時間の低下は，主にイオンの熱輸送特性の劣化による。一方，プラズマ電流の増加にほぼ比例した閉じ込め時間の改善は，イオン及び電子，両者の熱輸送特性の改善に起因する。また，イオンの熱輸送係数は，明かに密度依存性を有する。

高ベータ・ホロイダル（<3.5）プラズマにおいて得られた高イオン温度モードは，$r_a/a<0.5$の領域でのイオン熱輸送特性の改善による。また，その領域では，イオンの熱輸送係数は電子のそれとほぼ等しい値までに減少している。

那珂研究所：〒311-01 茨城県那珂郡那珂町大字向山801-1

Contents

目　　次

1. Introduction

As a tokamak plasma is auxiliary heated, the degradation in energy and particle confinement is generally observed. This plasma is so-called a L-mode. Although additionally heated plasmas of the L-mode are the most universal situation of a tokamak plasma, as well as saturated ohmically heated plasmas, it is presently uncertain which is responsible for the L-mode characteristics, electron or ion. Global confinement characteristics of such a L-mode are, however, well summarized as a power scaling, like INTOR89[1], in which the energy confinement time decreases in terms of the total heating power, Pabs, to the minus one-half power and improves almost linearly with increasing plasma current and has no or weak density dependence. The L-mode scaling also expresses the dependence of energy confinement time on the isotope and elongation effects. However, in order to extrapolate reliability to future plasma regimes, one needs to understand physics for local confinement in tokamaks, capable of describing global confinement scaling. The present work is intended to contribute to this important topic by analyzing profile data more systematically and by attempting to find mechanisms which are essential for the L-mode transport. In order to understanding the transport physics based on the theoretical background, it is very important to clarify what parameter dependencies the local transport has. Therefore, our study will be concentrated on studying the parameter dependence of local thermal diffusivities in L-mode plasmas, so dependencies of density, power and plasma current.

In this paper we present the results of an experimental study of the ion thermal diffusion process in JT-60. The experimental method used to obtain the ion temperature profiles is presented in Section 2. The transport analysis method is described in Section 3. Section 4 contains the experimental results and discussions. Finally, the main results are summarized in Section 5.

2. Diagnostics and Data Acquisition

A set of measured radial profiles relating with local transport analysis is briefly summarized. Schematic views of diagnostic instruments for radial profile measurements are shown in Fig. 1. The electron temperature profile was obtained from two Thomson scattering systems with 8 points in space and from the electron cyclotron emission (ECE) diagnostic with 28 points. Two Thomson scattering systems enable us to evaluate the profiles in the minimum time duration of 2 msec. The electron density profile obtained from Thomson scattering was cross-checked against the line electron densities obtained from the two chord far-infrared interferometers and one chord of 2 mm-μ wave interferometer close to the plasma center. The ion temperature profile measurements were obtained with toroidal rotation velocity profile measurements using a charge-ex-

change recombination spectrometer (CXRS) viewing across a nearly perpendicularly injected diagnostic neutral beam. The JT-60 CXRS diagnostic uses the heating neutral beams as diagnostic beams. It features one tangential line of sight, which intersects the heating beams, and a multi chord arrangement for profile measurements with 8 nearly tangential viewing lines which intersect the heating beams at major radii between 2.9 m and 3.8 m. The ion temperature measurements by CXRS presented in this paper are based on Doppler broadening of the n=8 to n=7 transition of C^{+5} at 5290.5 Å. The radiated power profile was measured from two bolometer array systems with 16 channel and 15 channel and determined by Abel inversion. The effective ionic charge, Z_{eff}, was estimated by two chord spectrometers for visible Bremsstrahlung emissions and assumed to be spatially constant. The particle confinement time is inferred from empirical scaling[2],

$$\tau_p = 0.05\left(\frac{\bar{n}_e}{10^{20}m^{-3}}\right)^{1}\left(\frac{P_h}{MW}\right)^{-0.5} \text{ sec} \qquad (1)$$

This scaling shows that τ_p decreases inversely with the electron density and in terms of the heating power to the minus half-power.

Figure 2 shows typical time evolutions of the central ion temperature, the line electron density and the diamagnetic measured stored energy of a L-mode, diverted discharge with I_p = 1.5 MA. Since the ion temperature from CXRS is obtained after subtracting the cold component level from measured spectrum, the JT-60 CXRS diagnostic is restricted to the duration in which the cold component level is estimated by stopping the diagnostic beam injection for 50 msec and could be interpolated, as shown in Fig. 2. NB heating starts at 5.5 second and lasts in 2 seconds with the power of ~ 15 MW. The central temperature of ion and electron vary little during heating phase. The radiated power increases by heating, but remains at about 10-15 % of the heating power. The diamagnetic measured stored energy and the line electron density reach steady state quickly. The density rises initially at a slow rate, due mainly to the beam fueling, then reaches at a steady state. So, the profile data for transport analysis are taken at this steady state of 7.1 sec. Figure 3 shows profile data of ion temperature, electron temperature, radiated power, and electron density at that steady state. It is found that the radiated power profile is fairly flat, which is commonly observed in divertor discharges.

Diagnostics data measured in the space of (R,Z) are mapped to flux surfaces calculated by the magnetic fitting / MHD equilibrium code[3] and are reduced to profile data as a function of effective minor radius r, which is defined by $r = \sqrt{V/2\pi^2 R_0}$ (V; volume, R_0 ; major radius). These profile data in the r space are least-square-fitted by using a proper functional form. As the standard, we

select the following two types of fitting functions, depending on the number of available data points,

$$f(\rho) = (f_0 - f_a)\{1 - \rho^2 + \alpha\rho^2(1 - \rho) + \beta\rho^2(1 - \rho^2)\} + f_a \quad (2)$$

$$f(\rho) = (f_0 - f_a)(1 - \rho^2)^{\alpha} + f_a \quad (3)$$

where $\rho = r/a$. 'a' is the minor radius at a plasma boundary flux surface. 'f_0' and 'f_a' are central and boundary values, respectively. All these profile data are stored in the transport data base "SCOOP DATA" together with magnetic data and so on.

3. Analysis Procedure

The particle and energy transport have been analyzed by the $1\frac{1}{2}$D, steady-state transport analysis code SCOOP[4] using the SCOOP DATA. For these fitting data and the effective charge state value, which is assumed to be constant in the plasma, profiles of NBI power deposition, the fast ion density and the toroidal momentum input are calculated by the Orbit-Following Monte-Carlo method and finally the proton density profile is evaluated taking into account of the fast ion density: Note that the effective ionization crosssection of fast neutrals with fast ions is the almost same as the one with bulk proton ions in the energy range of JT-60 NBI. The first ion density calculated by the OFMC code, in which the particle diffusion is not considered, gives a good approximation. Figure 4 shows the effect of particle diffusion on fast ion slowing-down process. Even if the large particle diffusion is considered ($\tau_s D/a^2 = 0.5$), the fast ion density still remains about 60 % of these in the case of no-diffusion. Therefore, the diffusion of fast ions was neglected as the first approximation in our analyses.

Assuming a steady state and using profile data, the thermal diffusivities of electron and ion, and the momentum diffusivity are determined as;
the electron thermal diffusivity,

$$\chi_e(r) = \frac{-\frac{3}{2}\Gamma_e T_e + \frac{1}{r\langle|\nabla r|^2\rangle}\int_0^r r\,dr(P_J + P_{NBe} + Q_{ei} - P_R)}{-n_e\frac{\partial T_e}{\partial r}} \quad (4)$$

the ion thermal diffusivity,

$$\chi_i(r) = \frac{-\frac{3}{2}\Gamma_i T_i + \frac{1}{r\langle|\nabla r|^2\rangle}\int_0^r r dr (P_{NBi} - Q_{ei} - P_{CX})}{-n_i \frac{\partial T_i}{\partial r}} \tag{5}$$

and the momentum diffusivity,

$$\chi_\phi(r) = \frac{-\rho_i \Gamma_i R V_\phi + \frac{1}{r\langle|\nabla r|^2\rangle}\int_0^r T r dr}{-\rho_i R \frac{\partial V_\phi}{\partial r}} \tag{6}$$

where P_J is the joule heating power density profile, P_{NBe} and P_{NBi} neutral beam heat deposition profiles to electrons and ions, respectively, Q_{ei} is the electron-ion energy transfer term, and P_R and P_{CX} are the radiated power and charge-exchanged energy loss terms. Γ_e and Γ_i are the particle fluxes of electrons and ions, respectively. The coefficient in the convective term of energy balance equations is taken as 3/2, though there is a divergence of opinion associating with this coefficient [5],[6]. In the momentum diffusivity $\rho_i(=\sum m_i n_i)$ is the local mass density, and $\omega(=RV_\phi)$ the angular velocity. V_ϕ is the toroidal rotation velocity. T is the torque density from sources due to collision, beam-thermalization, and ionization, and from the loss due to charge-exchange in the slowing-down process.

From the steady particle balance equation, the ion particle flux, Γ_i, is given by,

$$\Gamma_i(r) = \frac{1}{r\langle|\nabla r|^2\rangle}\int_0^r (S_n + S_{NB}) r dr \tag{7}$$

where S_n and S_{NB} are particle sources from neutrals estimated by the particle confinement time and due to the beam fueling, respectively. With the assumptions of the electrical neutrality of a plasma and of one ionic impurity specie as a dominant impurity, the electron density is

$$n_e = n_i + n_f + Z_k n_k \tag{8}$$

where n_i is the thermalized ion density, n_f the fast ion density, and n_k the impurity ion density with fully stripped ionic charge state of Z_k.

If the toroidal electric field is assumed to be radially constant, the current profile is

$$j_{//} = \frac{1}{\eta}\frac{v_l}{2\pi R_0} \tag{9}$$

where v_l is the loop voltage and η the neoclassical resistivity [7]. The Joule input power is evaluated as,

$$\langle \mathbf{J}\cdot\mathbf{E}\rangle = \eta j_\varphi j_{//} \tag{10}$$

where

$$j_\varphi = \frac{1}{\mu_0}\frac{1}{r}\frac{\partial}{\partial r}\left[R_0^2\left\langle\left|\frac{\nabla r}{R}\right|^2\right\rangle r B_\theta\right] \tag{11}$$

and

$$B_\theta = \frac{\mu_0}{r}\left\langle\frac{1}{R^2}\right\rangle^{-1}\left\langle\left|\frac{\nabla r}{R}\right|\right\rangle \int_0^r \left\langle\frac{1}{R^2}\right\rangle j_{//}\, r dr \tag{12}$$

It is well known that for plasmas with the ion temperature close to the electron temperature, the uncertainty in the electron-ion energy exchange term makes it difficult to separate the electron and ion transport loss channels. However, large difference between electron and ion temperatures is not always a necessary condition to separate thermal transport channels. Dominant terms in the ion heat flux are the beam heating power and the energy equipartition terms. So, if the ion heating power is much grater than the energy equipartition, we can separately determine each thermal transport loss channel for plasmas with relatively small temperature differences between electrons and ions. And for many L-mode shots, the energy equipartition term is smaller than the beam heating power. Through our analyses, error bars on the computed diffusivities are evaluated for varying profile data in their error bars so that the diagnostic uncertainties of gradients and temperature differences become maximum.

4. Experiments and Transport Analyses

In order to study the thermal transport properties of L-mode plasmas, systematic experiments were performed in the wide regions of plasma parameters where, for divertor discharges, major radius, R_0 = 2.9 m, minor radius, a = 0.64 m, elongation, κ = 1.4, the plasma currents, I_p = 1.0 ~ 1.8 MA, the line averaged electron density, $\bar{n}_e = 1.2 \sim 5.0\times10^{19}$ m^{-3}, total input powers including Joule and neutral beams heating powers, P_{abs} = 1.3 ~ 16.7 MW, and for limiter discharges, R_0 = 3.0 m, a = 0.88 m, κ = 0.96, I_p = 1.0 ~ 2.7 MA, $\bar{n}_e = 1.2 \sim 6.5\times10^{19}$ m^{-3}, and P_{abs} = 3.0 ~ 17.4 MW. The toroidal filed, B_t is 4.5 T throughout experiments. The plasma configurations are slightly shifted into 0.1 ~ 0.2 m inside, compared with normal discharge configurations [8], for better accessibility of diagnostics to the center region of plasmas. The characteristics

feature of the consistent data set for limiter discharges is that the electron densities are increasing with heating power due to the neutral beam particle source. On the other hands, for divertor discharges, the power scan could be performed with almost constant electron densities ($3.0\times10^{19} \leq \bar{n}_e \leq 4.0\times10^{19}$ m^{-3}).

First, the density dependence of the kinetic stored energy is considered. Figure 5-(a) shows the diamagnetic measured stored energy against the density for 1.0 MA, divertor discharges with the fixed beam power of 2.1 to 2.6 MW. As the L-mode scaling indicates, the diamagnetic stored energy is independent on the density. However, the kinetic stored energy, which is estimated by subtracting the unthermalized beam component from the diamagnetic one, apparently increases with a rise of the density, as shown in Fig. 5-(a). So, there should be some improvements in the plasma confinement, as the density increases. The thermal diffusivities at half radii of plasmas indicate the reduction of the ion thermal diffusivity with increasing the density (Fig. 5-(b)). On the other hands, the electron thermal diffusivity does not seem to be reduced. Therefore, the improvement in the ion transport may account for the density dependence of the kinetic stored energy. Even in much higher heating power region of 11.1 to 13.7 MW for 1.5 MA, divertor discharges, we can also see that the kinetic stored energy increases with the density (Fig. 6-(a)). And the ion thermal diffusivity still seems to be a decreasing function of the density (Fig. 6-(b)), although the separation of the transport loss channel becomes to be slightly difficult because of high density.

In order to find out what changes in the transport, when the density increases, the temperature profiles of electron and ion are shown in Fig. 7, for two discharges with different densities of 1.4×10^{19} m^{-3} and 3.1×10^{19} m^{-3}. As the density increases from 1.4×10^{19} m^{-3} to 3.1×10^{19} m^{-3}, the electron temperature decreases over the whole radius (Fig. 7-(a)). On the other hands, the ion temperature moderately decreases, as shown in Fig. 7-(b). Figure 8 shows the comparison of the neutral beam deposition profiles. Since the JT-60 neutral beams are nearly perpendicularly injected, the deposition profile in higher density is not much different from that in the lower density. Therefore, the difference in temperature profiles shown in Fig. 7 are not caused by the difference in the neutral beam deposition profiles but by the transport process depending on the electron density. For these discharges, the inferred χ_i and χ_e profiles are shown in Fig. 9. When the density increases, χ_i remarkably decreases by a factor of 10 inside the half radius. On the other hands, χ_e does not show the reduction that is corresponding to the temperature degradation over the whole radius, as the density increases. This reduction in χ_i suggests that the density dependence of the kinetic stored energy is mainly due to the improvement in the ion thermal transport with increasing the density. This density dependence, however, makes the transport study confusing. In the local transport study presented we have paid carefully attention to the density.

Next, the power dependence of the confinement, which is the most basic parameter dependence appeared in the L-mode scaling, is studied. Figure 10-(a) presents the kinetic stored energy, W_k, including the beam component, W_b, against the diamagnetic measured stored energy, W_{dia}, for 1.0 MA, divertor discharges in the density region of $\bar{n}_e = 3.0 \sim 4.4\times10^{19}$ m^{-3}, where only two shots have the density higher than 4.0×10^{19} m^{-3}, accompanied by higher heating power of around 15 MW, and the other shots are in the relatively narrow density region of $3.0 \sim 4.0\times10^{19}$ m^{-3}. The reasonable agreement shown in Fig. 10-(a) gives us confidence that we have an accurate estimate of the kinetic stored energy, as well as the beam component evaluated. In order to determine the each dependence of the stored energy components of ions, electrons, and unthermalized ions on the total heating power, the kinetic stored energy is decomposed into three components of ion, electron, and unthermalized ion, and shown against the total heating power in Fig. 10-(b). From this figure, it is found that the parts of electron and unthermalized ion increase with a rise of heating power. The ion stored energy, however, slightly increases and the increment of ion energy to the total power is only one-third of those of electron. Figure 10-(c) shows the change of Z_{eff} value followed by the increase of total heating power. As the power is grater than 15 MW, the value of Z_{eff} increases nonlinearly due to the radiative enhancement sublimation at the edge of the divertor plates [9]. Within a power of 10 MW, Z_{eff} is still less than two, in which a fraction of the ion density to the electron density is grater than 80 %. Therefore, the slight increase in the ion stored energy cannot be caused by proton dilution, for the power region less than 10 MW. It may be concluded that the deterioration of ion confinement will be responsible for the power degradation of the L-mode.

Local thermal transport analysis provide a better description of confinement properties of plasmas with substantially different heating powers. Thus, we describe radial transport analysis of the electron and ion thermal conductivities under several beam injection configurations with the low density of 1.0×10^{19} m^{-3} $\le \bar{n}_e \le$ 3.0×10^{19} m^{-3}, so that we can separate the electron and ion channels. Figure 11 shows thermal conductivities of ion and electron at a half radii of plasmas as a function of the total heating power, in which open symbols correspond to divertor discharges and closed one to limiter discharge. For both configurations with the plasma current of 1 MA (Fig. 11-(a)), the ion thermal conductivity significantly increases in proportional to the heating power and is about three times the electron thermal conductivity at around 9 MW, whiles the electron conductivity gradually increases with the power. This figure strongly suggests that the ion conduction loss plays a major role of energy loss mechanisms for low plasma current discharges of I_p = 1 MA.

On the other hands, in the case of 2 MA plasmas under limiter configurations (Fig. 11-(b)), the transport loss process seems to be fairly different from the low current case. The electron conductivity is found to be larger than that of the ion.

at low power level of 4 MW as shown in Fig. 11-(b). The ion thermal conductivity, however, still increases to a level comparable to the electron conductivities, following a rise of auxiliary heating power : Data points shown by bracket in Fig. 11-(b) are only presented as a reference for higher heating power, because the line average electron density for this shot is 4.0×10^{19} m^{-3} and out of the limitation. Interesting feature that can be seen in Fig. 11 is that the dominant loss channel is different at a low power region of around 4 MW, depending on the plasma current. For two discharges where the plasma current is 2 MA, the line average electron density is 2.3×10^{19} m^{-3}, and heating powers are respectively ~3.7 MW and ~6.3 MW, radially integrated power flows of electron and ion are shown in Figs. 12 and 13, in which conduction, P_{cnd}, is the dominant loss in the both electron and ion power balances. The energy equipartition, P_{eq}, and convection, P_{cnv}, remain small loss. In the electron power balance the radiative power loss, P_{rad}, becomes comparable to P_{cnd} at a peripheral region. In the case of lower heating power of ~3.7 MW (#10620), the joule input, P_{joule}, is still the dominant heating power in the electron power balance, comparing with auxiliary heating power. On the other hands, in the case of higher heating power of ~6.3 MW (#10643), P_{joule} and the additional heating power to electrons, P_{NB}^{e}, becomes comparable, and P_{joule} results in a small fraction of total input power. The energy exchange is so small that the input power must be carried out through each loss channel. Therefore, the large input power into the electron channel and small energy exchange term between the electron and ion mean that the large flow through the electron channel can carry out the most of input power. That is the reason why the electron conduction is larger than that of ion at a low power level. For these shots, the profiles of χ_e and χ_i are shown in Fig. 14. A comparison of profiles under different heating power levels shows that as the auxiliary heating power increases by a typical factor of ohmic power, the ion diffusivity is enhanced over the whole radius and the enhancement factor of neoclassical χ_i surprisingly increases by a factor of 13 to 36. On the other hands, χ_e shows little changes in magnitude. Again, come back to the power dependence, we can still say that even in a higher current of 2 MA, the ion loss channels increases as the heating power increases. Therefore, power degradation is mainly caused by enhanced ion thermal transport and starts only with a slight auxiliary heating power.

Next, we will study the plasma current dependence of the confinement which is not only another important feature of the L-mode scaling but also a key issue to extrapolate reliability to future plasma regimes. A plasma current scan from 1.0 MA to 2.0 MA was performed for limiter discharges at nearly constant heating power of 5.6 MW to 6.3 MW and the same Z_{eff} value of 3.9, though the line average electron density for 2.0 MA shot ($\bar{n}_e = 2.3\times10^{19}$ m^{-3}) is slightly higher than that for 1.0 MA discharge ($\bar{n}_e = 1.6\times10^{19}$ m^{-3}). The experimentally inferred

diffusivities of χ_i and χ_e are compared in Fig. 15. The small input power to the ion channel and the strong sensitivity to the difference in temperature of the energy exchange term in the ion power balance mean that the error in χ_i is very large indeed. Interestingly, however, despite the problems in determining χ_i, it seems that χ_i is somewhat improved across the entire plasma cross section as shown in Fig. 15-(a). The enhancement factor of the neoclassical χ_i at r/a=0.5 decreases from about 34 to 17, as the plasma current increases. The electron thermal diffusivity increases toward the plasma edge for high q discharge, as shown in Fig. 15-(b). Thus, the improvement in χ_e for plasma scans from 1.0 MA to 2.0 MA is clear at r=2a/3 where the plasma is dominantly confined. In spite of large error bars, the reduction of χ_i and χ_e allows the determination that both improvements in the ion and electron confinement with the increase of I_p are responsible for the origin of linear current scaling in L-mode confinement.

High central ion temperature up to 12 keV was obtained at high poloidal-beta plasmas with high power long pulse neutral beam heating. Plasma profiles for High-Ti mode and L-mode discharges are compared in Fig. 16; electron and ion temperature, electron density, and toroidal rotation velocity. In this High-Ti mode, extremely peaked ion temperature profiles and well peaked density profile were realized in a narrow range of I_p = 0.3 ~ 0.5 MA. The most remarkable feature is that the central ion temperature is about two times the electron temperature, decoupling of energy balance between electrons and ions. Another feature is the toroidal rotation velocity, which grows up to 75 to 100 km/s in a central region. Because of nearly balanced injection in JT-60, the rotation velocity in L-mode discharges is still small, as shown in Fig. 16-(d).

To study what changes in transport occur between High-Ti mode and L-mode discharges, comparisons of both discharges for χ_e and χ_i are performed in Fig. 17. We can see that χ_i is significantly reduced by a factor of 10 to 5 inside a half-radius, compared with that in the L-mode. However, there is little change in both χ_e. It is also found that the momentum diffusivity is comparable to χ_i and χ_e, around r/a = 0.4. Therefore, the improvement in χ_i is responsible for the High-Ti mode.

5. Summary

Local heat transport has been studied in auxiliary heated, JT-60 plasmas with emphasis on understanding the deteriorated confinement observed in L-mode plasmas. The systematic experiment and analysis have been carried out in L-mode phase of divertor (single null, lower X-point), and limiter discharges with hydrogen neutral beam heating ($P_{NB} \leq 18$ MW, $E_0 = 65 \sim 75$ keV) into hydrogen plasmas ($I_p = 1.0 \sim 2.7$ MA, $B_t = 4.5$ T, $\bar{n}_e = 1.2 \sim 6.5 \times 10^{19}$ m^{-3}), based on

sets of consistent experimental data including ion temperature profiles from CXRS measurements.

It is now generally acknowledged that heat flux through the ion channel may be important in determining confinement. The deterioration in the energy confinement time with increasing the auxiliary heating power, so called the power scaling, is mainly due to the degradation in ion energy transport. The confinement improvement as the plasma current increases is followed by both improvements in ion and electron transport properties. It is found that the ion thermal diffusivity has an approval dependence on the density. This cannot be excluded even at medium density.

The parameter dependence of χ_i will be illustrated with a rough picture that χ_i is a decreasing function of the density, but increases with a rise of the auxiliary heating power, and χ_i is improved with increasing plasma current. However, parameter dependence of χ_e is essentially indeterminate. This is because that in a hydrogen plasma, the ion anomalous transport is so dominant in the power balance that the electron transport is masked behind the ion transport characteristic.

High ion temperature ($T_i(0) \leq 12$ keV) L-mode plasmas are attained at high β_p up to 3.5. The centrally peaked ion temperature is significantly due to the improvement in ion transport property, which is reduced to the level of the electron thermal diffusivities.

Acknowledgements

We are indebted to the entire JT-60 team and in particular to the diagnostics and data management groups for providing the basic data for this study. The authors wish to thank Drs. T. Tuda and T. Takizuka for fruitful discussions. The continuing support of Drs. M. Yoshikawa, T. Iijima, S. Tamura, Y. Tanaka, H. Kishimoto and Y. Shimomura is gratefully acknowledged.

References

[1] P.N. Yushmanov, T. Takizuka, K.S. Riedel, O.J.W.F. Kardaun, J.G. Cordey, S.M. Kaye, D.E. Post, Nucl. Fusion **30** (1990), 1999.

[2] K.Yamada, et al., Nucl. Fusion **27** (1987) 1203.

[3] M. Azumi, et al., : A Fluid Numerical Code System for Tokamak Fusion Research, Proc. of 4th Int. Symp. Computing Methods in Applied Sciences and Engineering, (Paris, 1979) 335.

[4] T. Hirayama, et al., JAERI-M 88-043 (198) "Experimental Transport Analysis Code System in JT-60".

[5] D.F. Duchs, JET-R(89) 13, "3/2 or 5/2 for convective thermal transport?".

[6] D.W. Ross, Comments Plasma Phys., Cont. Fusion **12**, (1989), 155.

[7] S.P. Hirshman, R.J. Hawryluk, B. Birge, Nucl. Fusion **17** (1977) 611.

[8] H. Nakamura, T. Ando, H. Yoshida, S. Niikura, T. Nishitani, K. Nagashima, Nucl. Fusion, **20** (1988) 43.

[9] T.Sugie, K.Itami, H.Nakamura, et al., 13th International Conference on Plasma Physics and Controlled Nuclear Fusion Research, IAEA-CN-53/A-5-4,(Washington, 1990)

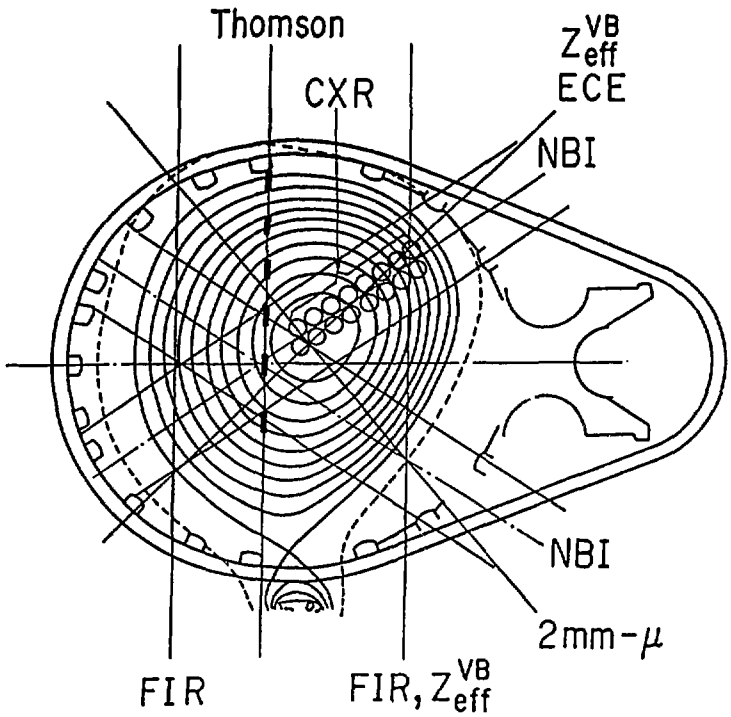

Fig. 1 Experimental set up of the JT-60 diagnostic systems; Thomson scattering and ECE for Te, CXRS for Ti, interferometers of two chord FIR and 2 mm-μ wave for $\bar{n}_e$, two channel spectrometers of visible bremsstrahlung for Z_{eff}, and nearly perpendicular injected beam lines.

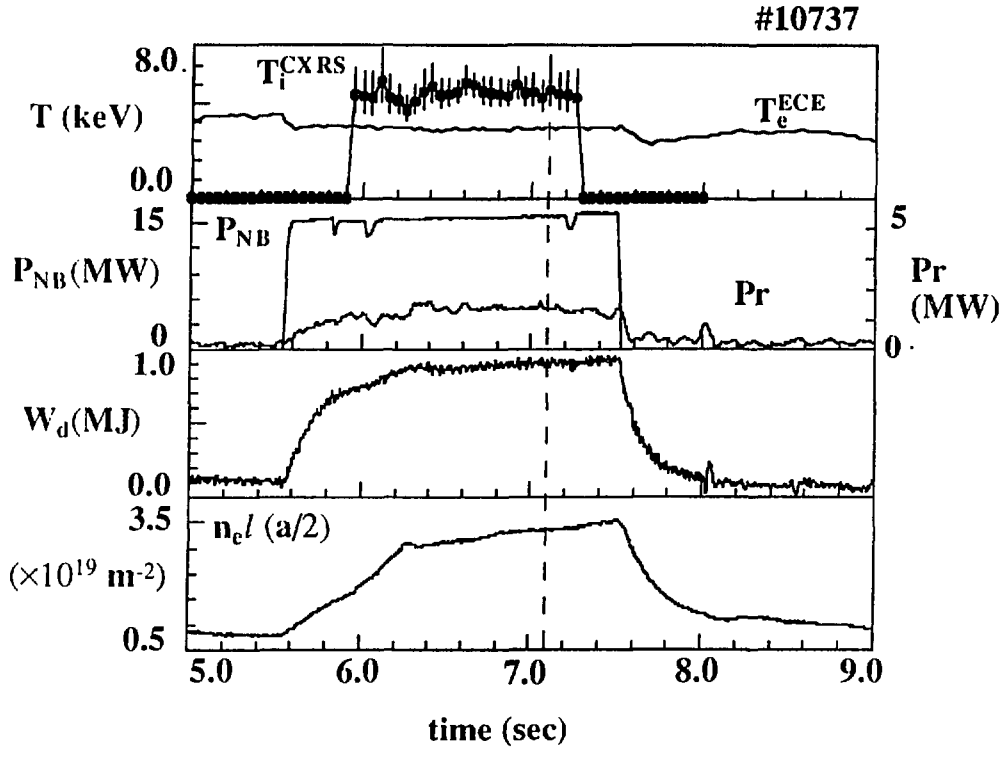

Fig. 2 Typical time evolutions of plasma parameters for the divertor discharge (#10737) with I_p=1.5 MA, $\bar{n}_e = 2.7\times10^{19}m^{-3}$, P_{abs} = 11.1 MW and Z_{eff} = 3.8: a) central temperatures of the ion and the electron from CXRS and ECE, respectively; b) neutral beam heating power and total radiation power; c) diamagnetic stored energy; d) the line electron density at r/a~1/2.

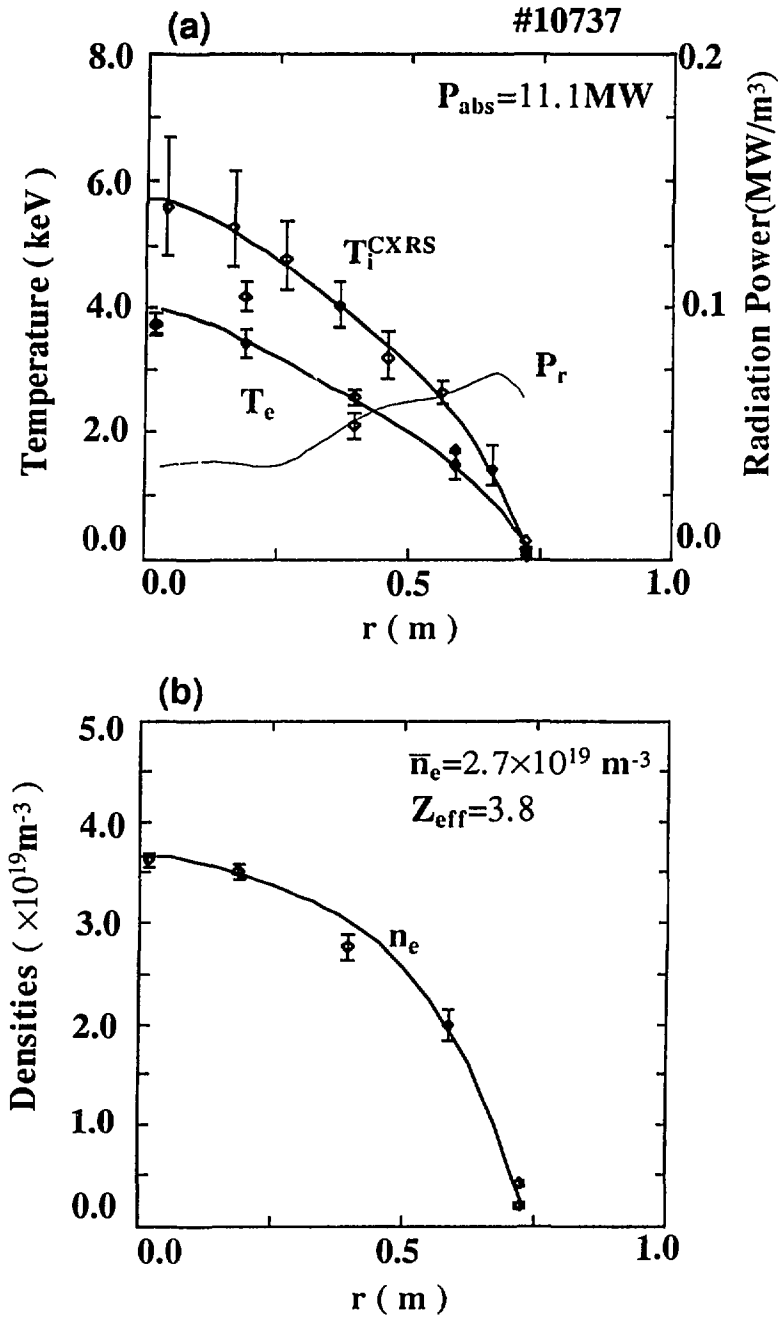

Fig. 3 Typical profile data of the divertor discharge (#10737) at a quasi-steady state of 7.1 sec: a) profiles of electron and ion temperatures, and radiation power; b) electron density profile.

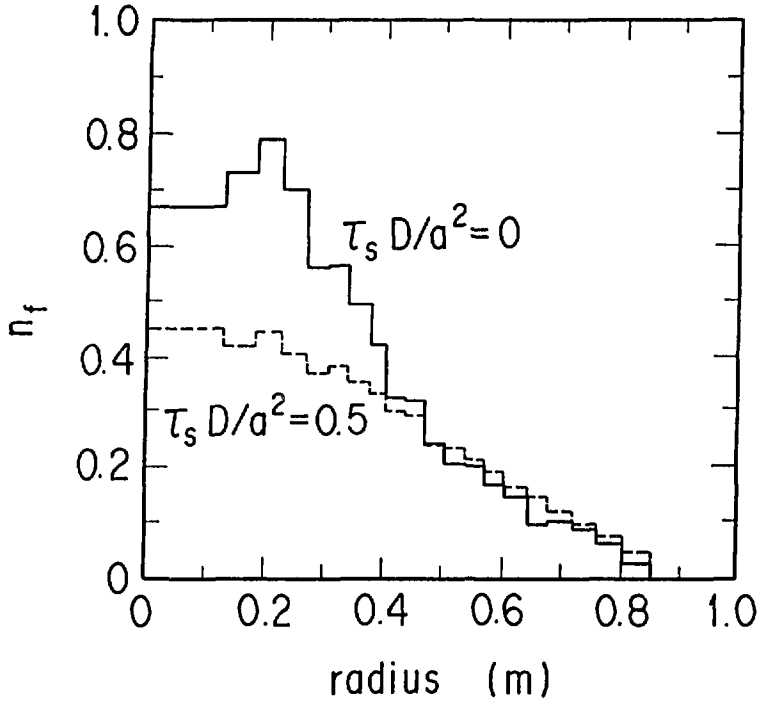

Fig. 4 Effect of particle diffusion on fast ions in slowing-down process. The beam acceleration energy is 75 keV. Normalized particle diffusion co efficient is assumed as $\tau_s D/a^2 = 0.5$, in which τ_s is the slowing-down time.

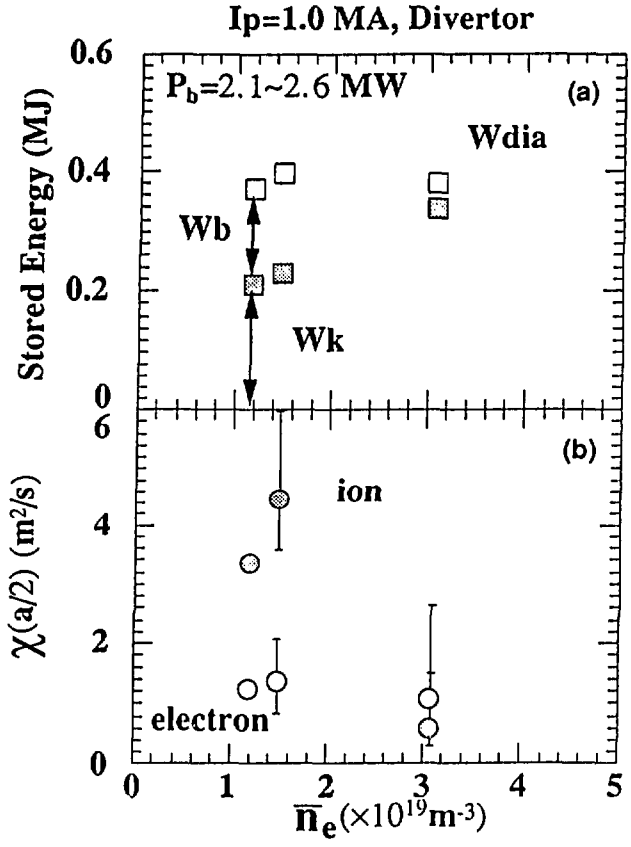

Fig. 5 Density dependencies of the diamagnetic measured stored energy, the kinetic stored energy, and the local thermal diffusivities of ions and electrons at half radii of plasmas with 1.0 MA, divertor configurations and the fixed beam powers of 2.1 MW to 2.6 MW: (a) the density dependencies of the diamagnetic stored energy, W_{dia} (open square symbols) and of the kinetic stored energy, W_k(closed square symbols), subtracted the beam component, W_b, from the W_{dia}; (b) the thermal diffusivities of ions (open circles) and electrons (closed circles) versus the line average electron densities.

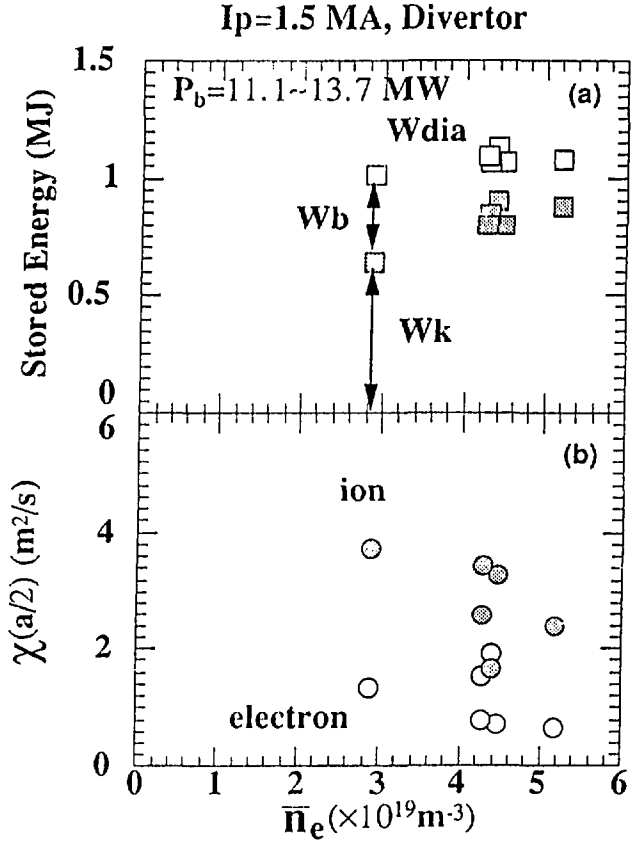

Fig. 6 Density dependencies of the diamagnetic measured stored energy, the kinetic stored energy, and the local thermal diffusivities of ions and electrons at half radii of plasmas with 1.5 MA, divertor configurations and the fixed beam powers of 11.1 MW to 13.7 MW: (a) the density dependencies of the diamagnetic stored energy, W_{dia} (open square symbols) and of the kinetic stored energy, W_k(closed square symbols), subtracted the beam component, W_b, from the W_{dia}; (b) the thermal dissusivities of ions (open circles) and electrons (closed circles) versus the line average electron densities.

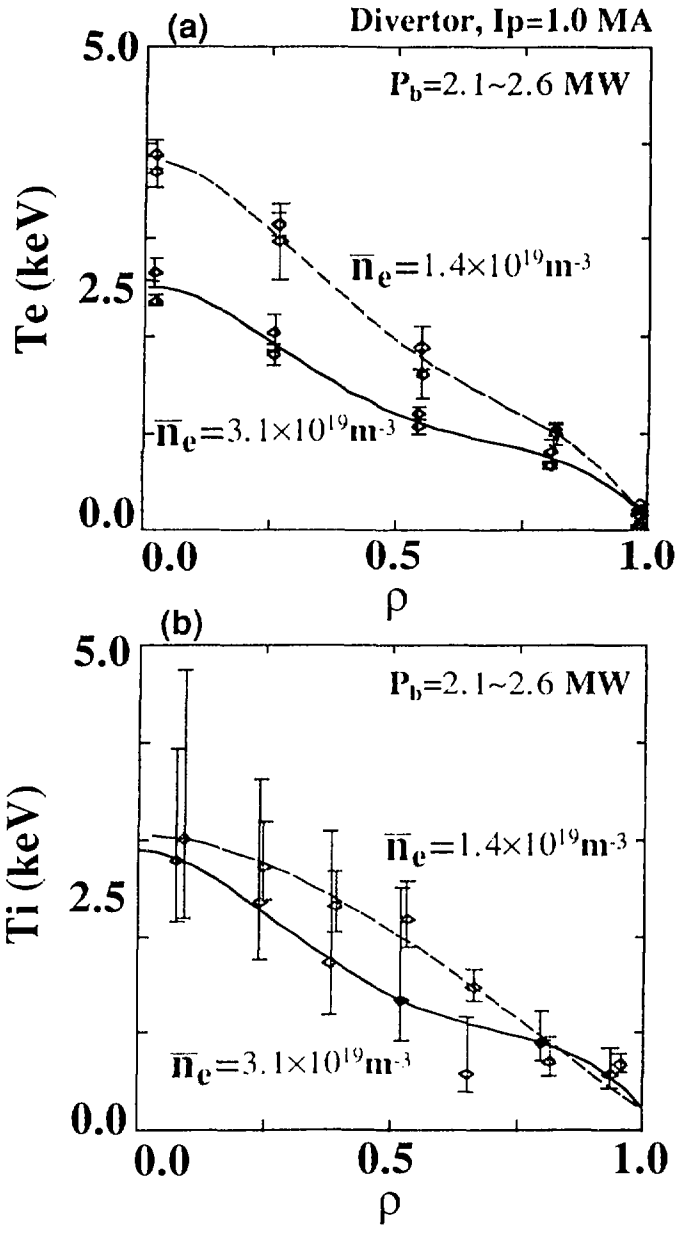

Fig. 7 Temperature profiles of 1.0 MA, divertor discharges for two different electron densities of 1.4×10^{19} m^{-3} (dashed lines) and 3.1×10^{19} m^{-3} (solid lines) with the fixed neutral beam heating powers of 2.1 MW to 2.6 MW: (a) the electron temperature profiles; (b) the ion temperature profiles.

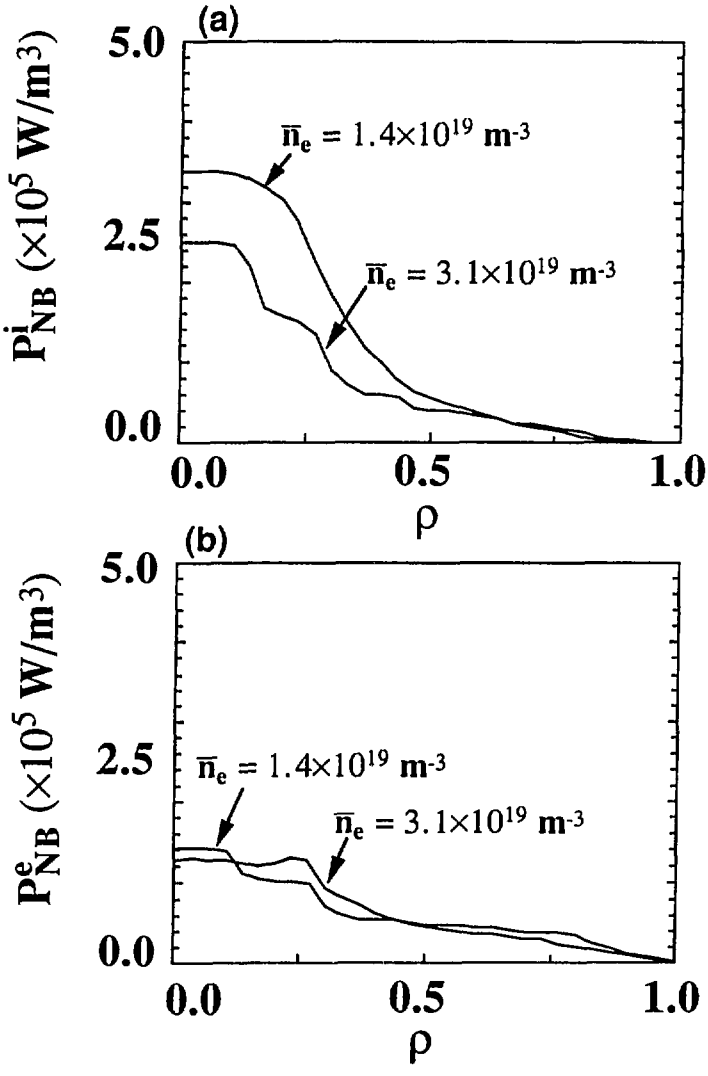

Fig. 8 Comparison of neutral beam deposition profiles of 1.0 MA, divertor discharges for two different electron densities of 1.4×10^{19} m^{-3} (dashed lines) and 3.1×10^{19} m^{-3} (solid lines) with the fixed neutral beam heating powers of 2.1 MW to 2.6 MW.

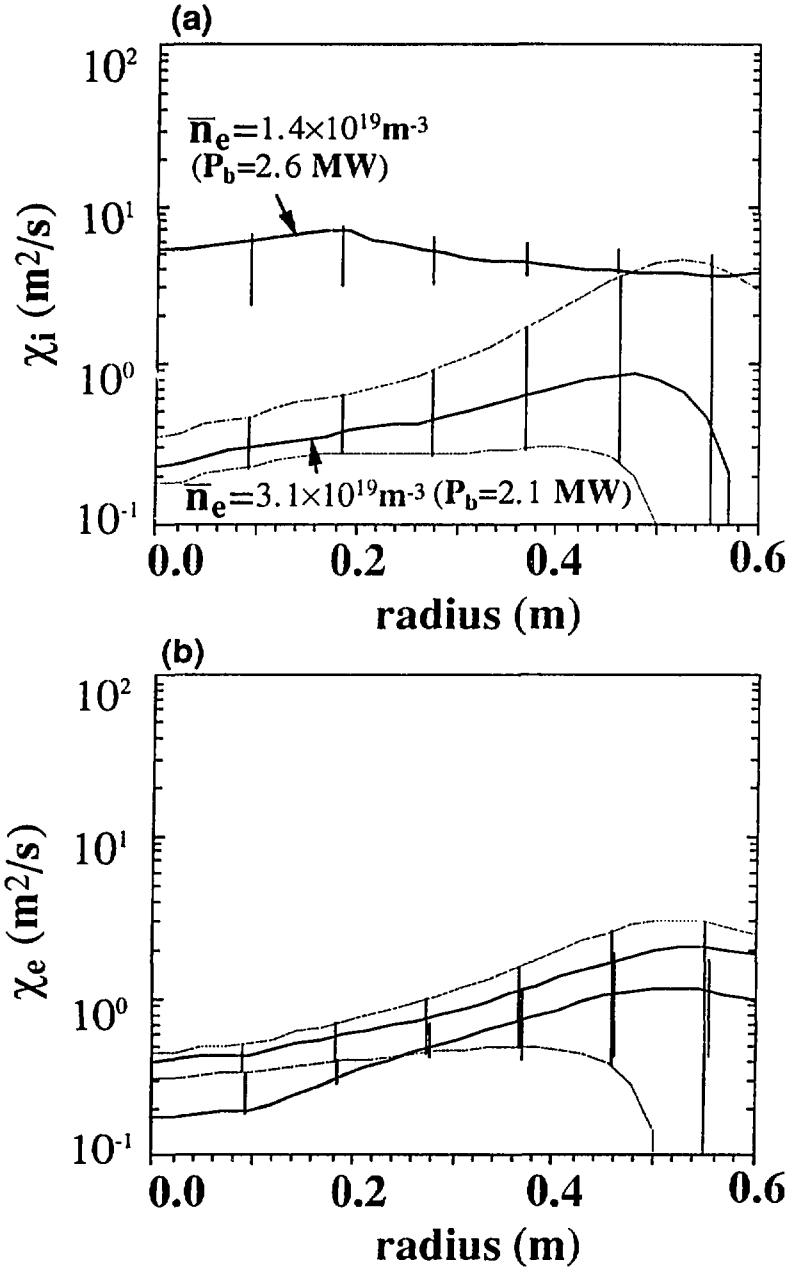

Fig. 9 The thermal diffusivity profiles of ions and electrons for 1.0 MA, divertor discharges with two different electron densities of 1.4×10^{19} m^{-3} (dashed lines) and 3.1×10^{19} m^{-3} (solid lines). The neutral beam heating powers are 2.1 MW to 2.6 MW: (a) the ion thermal diffusivity profiles ; (b) the electron thermal diffusivity profiles.

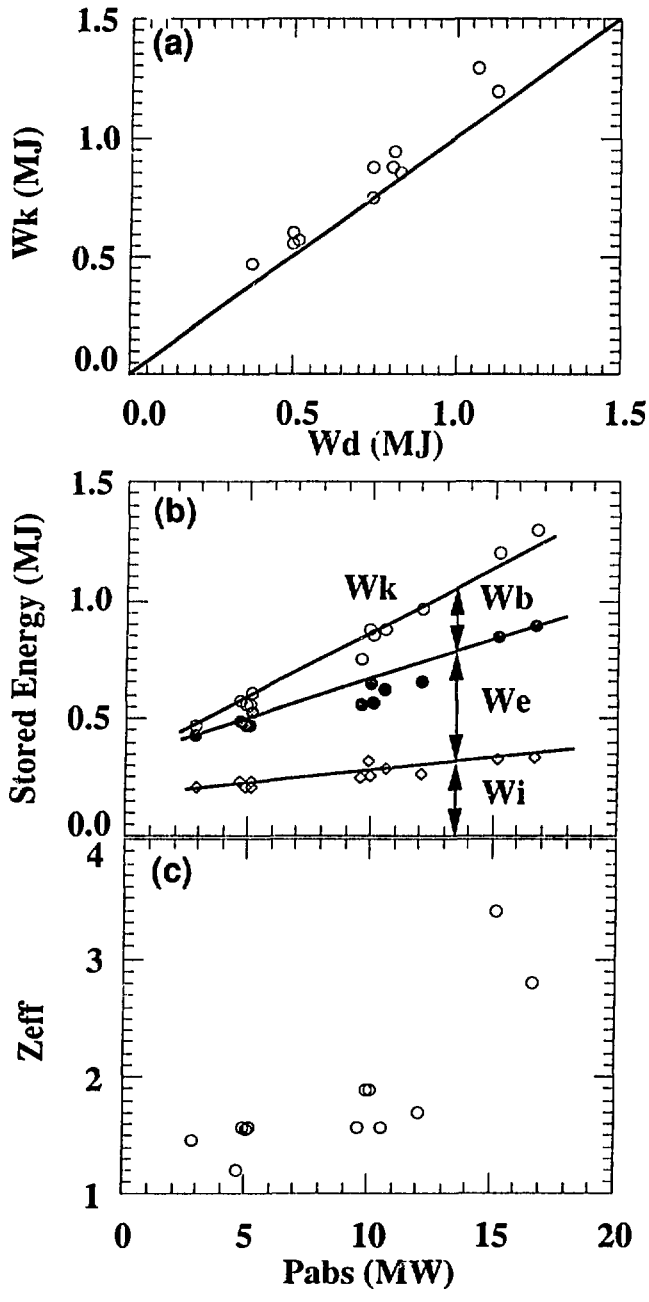

Fig.10 Dependence of the stored energy components on the total heating power for 1.0 MA, discharges with $\bar{n}_e = 3.0 \sim 4.4 \times 10^{19}$ m^{-3}: (a) comparison between kinetic stored energy, W_k, including the beam component, W_b, and the diamagnetic measured stored energy, W_{dia}: (b) dependence of stored energy components decomposed to ions, W_i electrons, W_e, and unthermalized ions, W_b on the total heating powers: (c) the values of Z_{eff} versus the total heating powers.

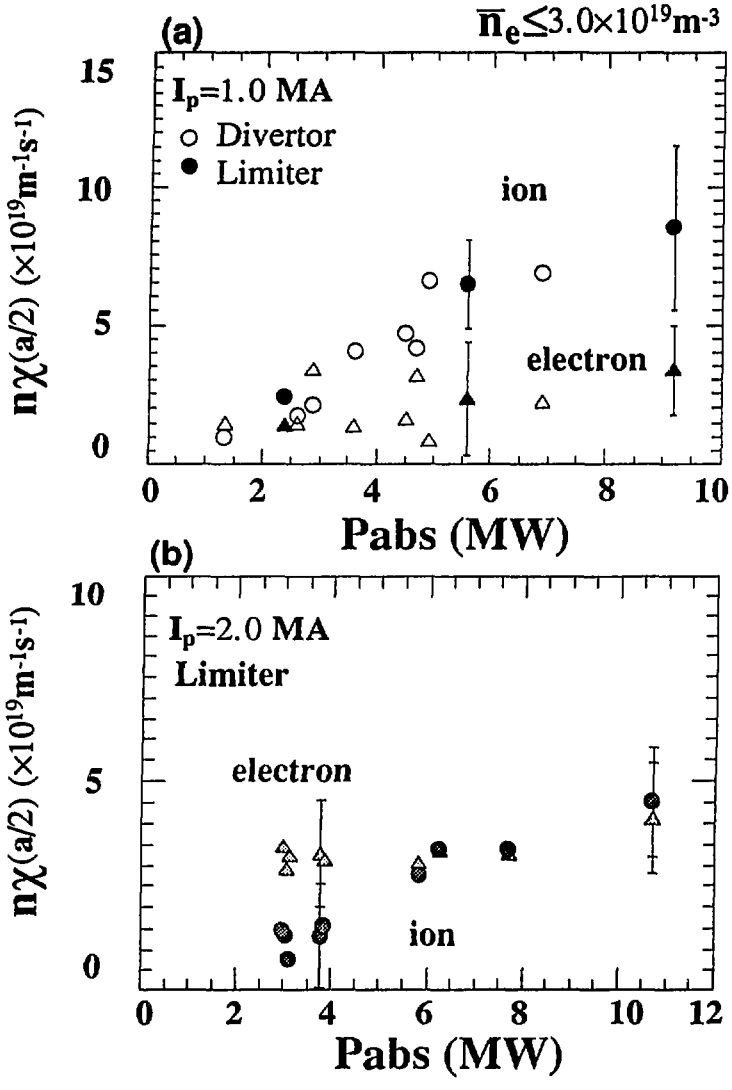

Fig. 11 Power dependence of thermal conductivities at half radii of plasmas under divertor and limiter configurations with low densities of 1.0×10^{19} $m^{-3} \leq \bar{n}_e \leq 3.0\times10^{19}$ m^{-3}: (a) for I_p = 1.0 MA, circle and triangular symbols are respectively the ion and electron thermal conductivities, respectively, in which open and closed symbols show divertor and limiter discharges, respectively.; (b) for I_p = 2.0 MA and limiter discharges, data points shown in bracket are only presented as a reference data for higher heating power, because the line average electron density is 4.0×10^{19} m^{-3}.

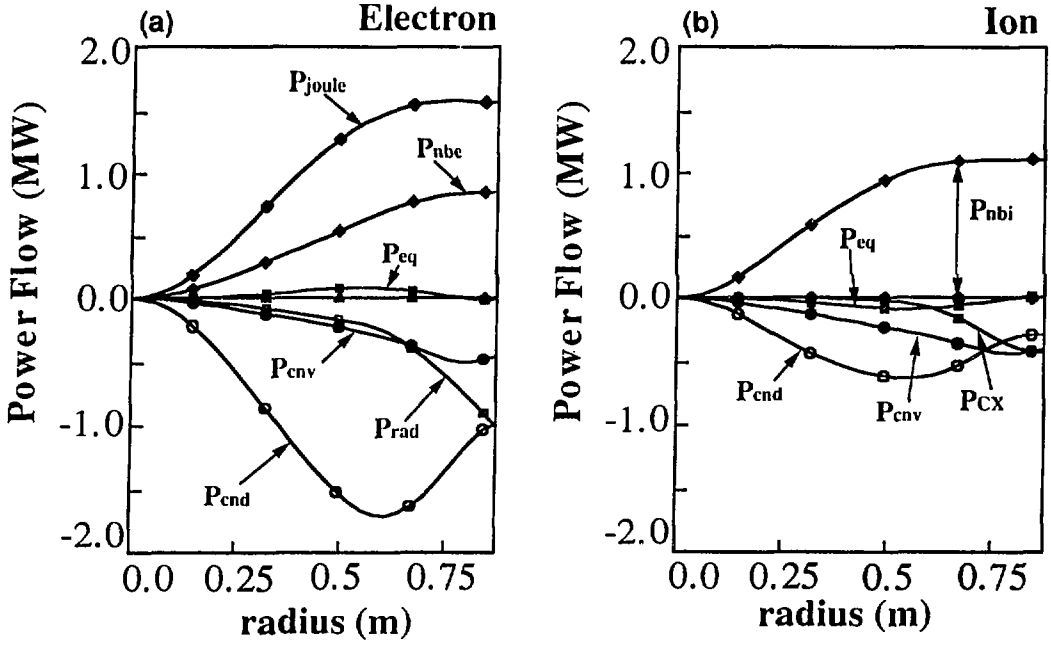

Fig.12 Radially integrated power flows of limiter discharge (#10620) with I_p = 2 MA, P_{abs} = 3.7 MW, $\bar{n}_e = 2.3\times10^{19}$ m^{-3} and Z_{eff} = 2.7 : (a) electron power flows, in which the electron conduction loss is P^e_{cnd}, the electron convection loss P^e_{cnv}, the energy exchange term P_{eq}, the radiation loss P_{rac}, the joule input power P_{joule}, and the neutral beam heating power to electrons P^e_{NB} ; (b) ion power flows, in which the ion conduction loss is P^i_{cnd}, the ion convection loss P^i_{cnv}, the charge exchange loss P_{CX}, and the neutral beam heating power to ions P^i_{NB}.

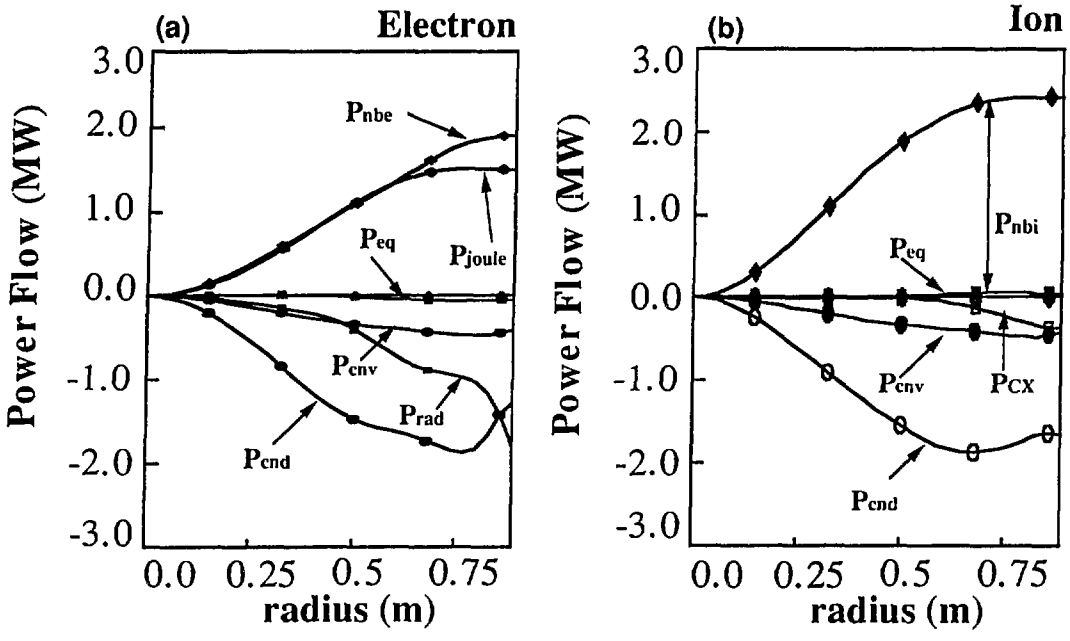

Fig. 13 Radially integrated power flows of limiter discharge (#10643) with I_p = 2 MA, P_{abs} = 6.3 MW, $\bar{n}_e = 2.3\times10^{19}$ m^{-3}, and Z_{eff} = 3.9 : (a) electron power flows; (b) ion power flows. The notations presented mean the same as those explained in Fig. 12.

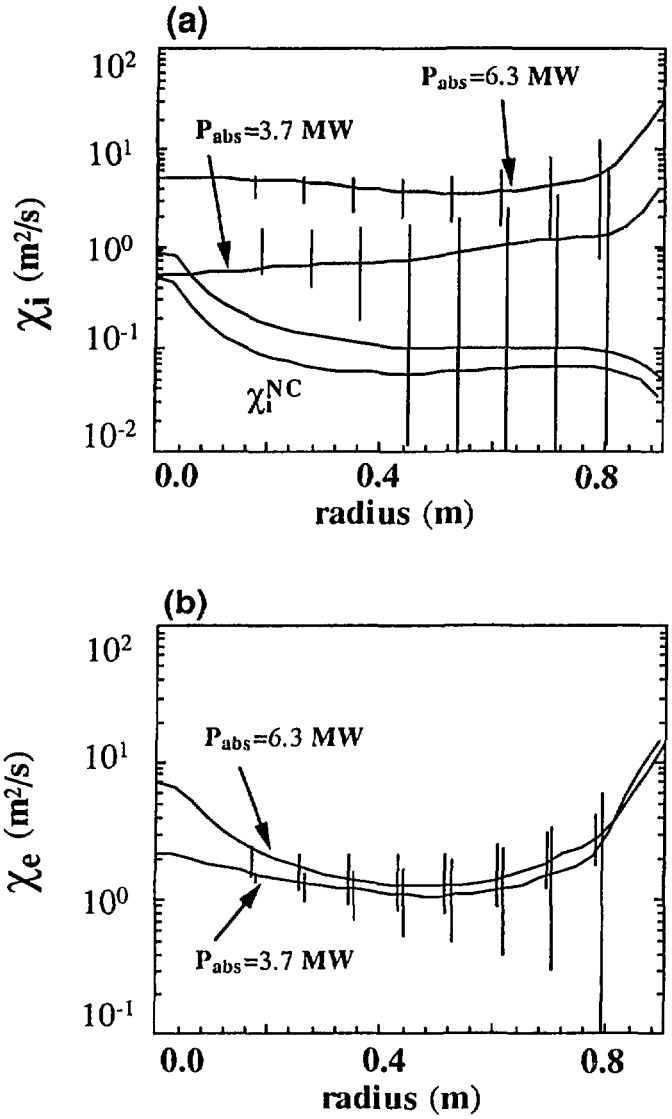

Fig. 14 The inferred diffusivity profiles of electron and ion under different heating powers. Two shots are #10620 and #10643, plasma parameters of which are referred in Figs. 12 and 13, respectively : (a) the inferred ion thermal diffusivity and the predicted neoclassical value, χ_i^{NC}; (b) the experimental value of the electron thermal diffusivity.

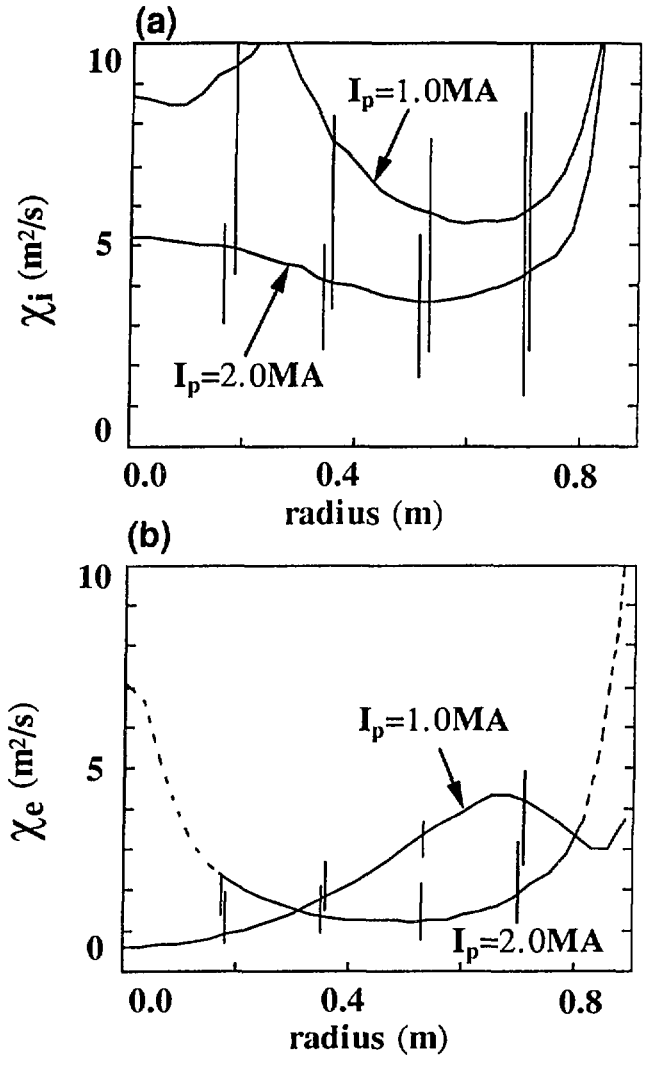

Fig. 15 Comparison of experimentally inferred χ_i and χ_e for plasma current scans from 1.0 MA to 2.0 MA at almost same heating power of 5.6 MW or 6.3 MW and constant Z_{eff} of 3.9. The line average electron densities are 1.6×10^{19} m^{-3} for I_p = 1.0 MA and 2.3×10^{19} m^{-3} for I_p = 2.0 MA: (a) ion thermal diffusivity profiles; (b) electron thermal diffusivity profiles.

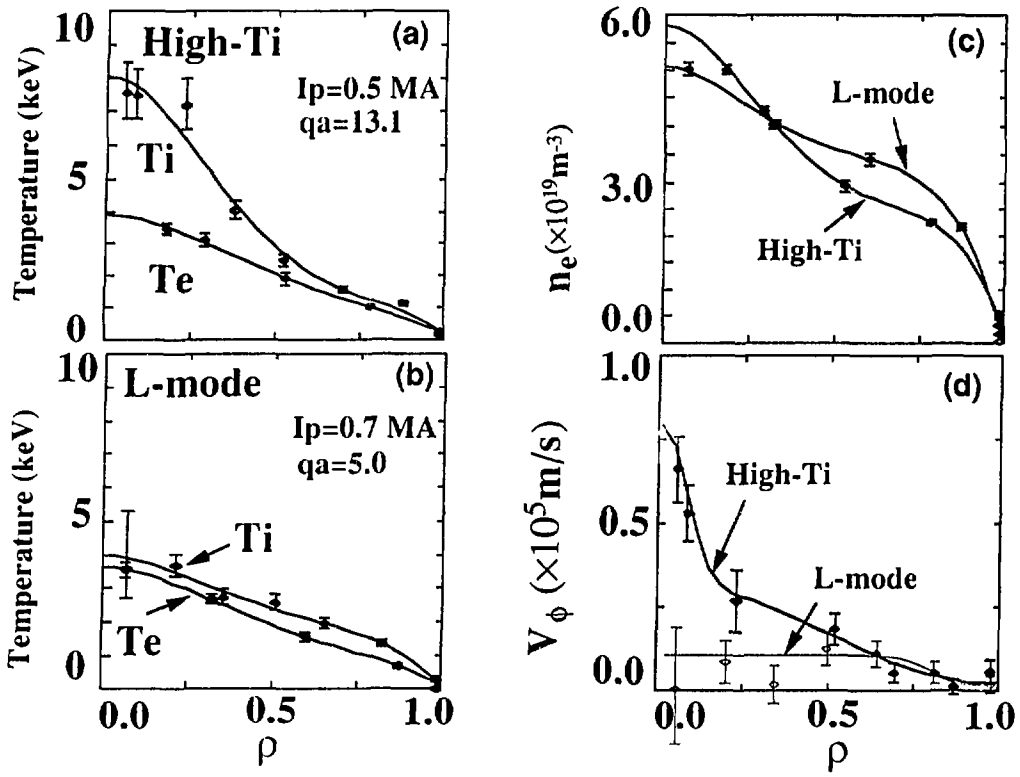

Fig. 16 Comparison of plasma profiles between High-Ti mode and L-mode discharges: (a) electron and ion temperature profiles for High-Ti mode discharge with I_p = 0.5 MA, B_t = 4.5 T, q_a = 13.1, P_{abs} = 18 MW, and $\bar{n}_e = 3.5\times10^{19}$; (b) electron and ion temperature profiles for L-mode discharge with I_p = 0.7 MA, B_t = 3.5, q_a = 5.0, P_{abs} = 18 MW, and $\bar{n}_e = 3.5\times10^{19}$ m^{-3}; (c) electron density profiles, in which peaking factors of density profile are 2.3 for High-Ti mode and 1.7 for L-mode, respectively; (d) the rotation velocity profiles.

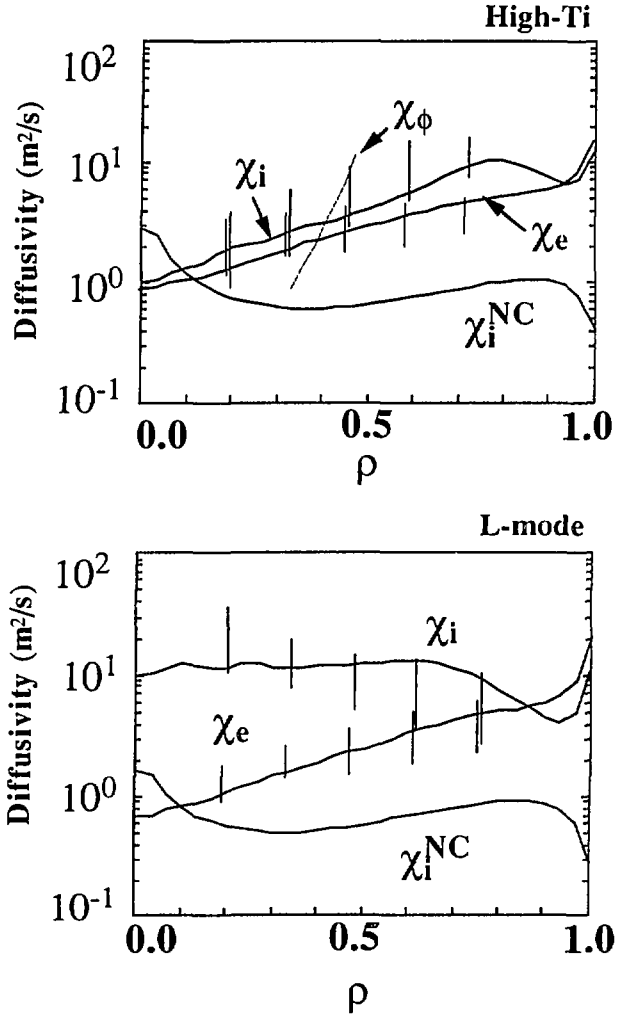

Fig. 17 Comparison of experimentally inferred χ_e, χ_i, and χ_ϕ for the High-Ti mode and L-mode discharges: (a) High-Ti mode discharge; (b) L-mode discharge.

国際単位系 (SI) と換算表

表 1　SI 基本単位および補助単位

量	名称	記号
長さ	メートル	m
質量	キログラム	kg
時間	秒	s
電流	アンペア	A
熱力学温度	ケルビン	K
物質量	モル	mol
光度	カンデラ	cd
平面角	ラジアン	rad
立体角	ステラジアン	sr

表 2　SI と併用される単位

名称	記号
分，時，日	min，h，d
度，分，秒	°，′，″
リットル	l，L
トン	t
電子ボルト	eV
原子質量単位	u

1 eV = 1.60218 × 10^{-19} J

1 u = 1.66054 × 10^{-27} kg

表 3　固有の名称をもつ SI 組立単位

量	名称	記号	他の SI 単位による表現
周波数	ヘルツ	Hz	s^{-1}
力	ニュートン	N	m·kg/s^2
圧力，応力	パスカル	Pa	N/m^2
エネルギー，仕事，熱量	ジュール	J	N·m
工率，放射束	ワット	W	J/s
電気量，電荷	クーロン	C	A·s
電位，電圧，起電力	ボルト	V	W/A
静電容量	ファラド	F	C/V
電気抵抗	オーム	Ω	V/A
コンダクタンス	ジーメンス	S	A/V
磁束	ウェーバ	Wb	V·s
磁束密度	テスラ	T	Wb/m^2
インダクタンス	ヘンリー	H	Wb/A
セルシウス温度	セルシウス度	℃	
光束	ルーメン	lm	cd·sr
照度	ルクス	lx	lm/m^2
放射能	ベクレル	Bq	s^{-1}
吸収線量	グレイ	Gy	J/kg
線量当量	シーベルト	Sv	J/kg

表 4　SI と共に暫定的に維持される単位

名称	記号
オングストローム	Å
バーン	b
バール	bar
ガル	Gal
キュリー	Ci
レントゲン	R
ラド	rad
レム	rem

1 Å = 0.1 nm = 10^{-10} m

1 b = 100 fm^2 = 10^{-28} m^2

1 bar = 0.1 MPa = 10^5 Pa

1 Gal = 1 cm/s^2 = 10^{-2} m/s^2

1 Ci = 3.7 × 10^{10} Bq

1 R = 2.58 × 10^{-4} C/kg

1 rad = 1 cGy = 10^{-2} Gy

1 rem = 1 cSv = 10^{-2} Sv

表 5　SI 接頭語

倍数	接頭語	記号
10^{18}	エクサ	E
10^{15}	ペタ	P
10^{12}	テラ	T
10^9	ギガ	G
10^6	メガ	M
10^3	キロ	k
10^2	ヘクト	h
10^1	デカ	da
10^{-1}	デシ	d
10^{-2}	センチ	c
10^{-3}	ミリ	m
10^{-6}	マイクロ	μ
10^{-9}	ナノ	n
10^{-12}	ピコ	p
10^{-15}	フェムト	f
10^{-18}	アト	a

(注)

1. 表 1 ～ 5 は「国際単位系」第 5 版，国際度量衡局 1985 年刊行による。ただし，1 eV および 1 u の値は CODATA の 1986 年推奨値によった。
2. 表 4 には海里，ノット，アール，ヘクタールも含まれているが日常の単位なのでここでは省略した。
3. bar は，JIS では流体の圧力を表わす場合に限り表 2 のカテゴリーに分類されている。
4. EC 閣僚理事会指令では bar，barn および「血圧の単位」mmHg を表 2 のカテゴリーに入れている。

換　算　表

力	N(=10^5 dyn)	kgf	lbf
	1	0.101972	0.224809
	9.80665	1	2.20462
	4.44822	0.453592	1

粘度　1 Pa·s(N·s/m^2) = 10 P(ポアズ)(g/(cm·s))

動粘度　1 m^2/s = 10^4 St(ストークス)(cm^2/s)

圧力	MPa(=10 bar)	kgf/cm^2	atm	mmHg(Torr)	lbf/in^2(psi)
	1	10.1972	9.86923	7.50062 × 10^3	145.038
	0.0980665	1	0.967841	735.559	14.2233
	0.101325	1.03323	1	760	14.6959
	1.33322 × 10^{-4}	1.35951 × 10^{-3}	1.31579 × 10^{-3}	1	1.93368 × 10^{-2}
	6.89476 × 10^{-3}	7.03070 × 10^{-2}	6.80460 × 10^{-2}	51.7149	1

エネルギー・仕事・熱量	J(=10^7 erg)	kgf·m	kW·h	cal(計量法)	Btu	ft·lbf	eV
	1	0.101972	2.77778 × 10^{-7}	0.238889	9.47813 × 10^{-4}	0.737562	6.24150 × 10^{18}
	9.80665	1	2.72407 × 10^{-6}	2.34270	9.29487 × 10^{-3}	7.23301	6.12082 × 10^{19}
	3.6 × 10^6	3.67098 × 10^5	1	8.59999 × 10^5	3412.13	2.65522 × 10^6	2.24694 × 10^{25}
	4.18605	0.426858	1.16279 × 10^{-6}	1	3.96759 × 10^{-3}	3.08747	2.61272 × 10^{19}
	1055.06	107.586	2.93072 × 10^{-4}	252.042	1	778.172	6.58515 × 10^{21}
	1.35582	0.138255	3.76616 × 10^{-7}	0.323890	1.28506 × 10^{-3}	1	8.46233 × 10^{18}
	1.60218 × 10^{-19}	1.63377 × 10^{-20}	4.45050 × 10^{-26}	3.82743 × 10^{-20}	1.51857 × 10^{-22}	1.18171 × 10^{-19}	1

1 cal = 4.18605 J (計量法)

= 4.184 J (熱化学)

= 4.1855 J (15 °C)

= 4.1868 J (国際蒸気表)

仕事率　1 PS (仏馬力)

= 75 kgf·m/s

= 735.499 W

放射能	Bq	Ci
	1	2.70270 × 10^{-11}
	3.7 × 10^{10}	1

吸収線量	Gy	rad
	1	100
	0.01	1

照射線量	C/kg	R
	1	3876
	2.58 × 10^{-4}	1

線量当量	Sv	rem
	1	100
	0.01	1

(86 年 12 月 26 日現在)